SETCOR
Conferences & Exhibitions

The International Surfaces, Coatings and Interfaces Conference

SurfCoat Korea 2018

March 28 to 30, 2018, Incheon - Korea

Conference Proceedings

DOI: https://doi.org/10.26799/cp-surfcoatkorea2018

Proceedings of SurfCoat Korea 2018 International Conference
Incheon, Rep. Of Korean, March 28 - 30, 2018
DOI: https://doi.org/10.26799/cp-surfcoatkorea2018

Industrial X-ray Fluorescence Coating Thickness Analyzer Application for Phosphate Coating Thickness on Steel

Aleksander Sokolov[1], Jelena Hasikova[1], Aleksej Pecerskis[1], Vladimir Gostilo[1]

[1] Baltic Scientific Instruments,

Ganibu dambis 26, LV-1005, Riga, Latvia, office@bsi.lv

KY Lee[2], HB Jung[2], JH Lim[2]

[2] Euro Science

Sangdaewon-Dong, Seongnam Woolim Lion's Valley 1-cha Rm815, Dunchon-daero 457 bun-gil 27, Jungwon-Gu, Seongnam city, zip)462-806 Korea, kylee@euroscience.co.kr

Abstract
The results of industrial application of an online X-ray fluorescence coating thickness analyser for measuring the thickness of phosphate coatings on moving steel strips are considered in the article. The target range of coating thickness to be measured is from tens to hundreds of mg/m^2 in a measurement time of 10 seconds. The measurement accuracy observed during long-duration factory acceptance test was 10-15%. The coating thickness analyser consists of two XRF gauges, mounted above and below the steel strip and capable of moving across the moving strip, system for their suspension and relocation and electronic control unit. Fully automated software was developed to automatically and continuously (24/7) control both gauges, scanning both sides of the steel strip, develop and test methods for measuring new coatings. It allows to perform offline storage and retrieval of the measurement results, remotely control the analyser components and measurement modes from a control room. The developed XRF coating thickness analyser can also be used for real-time measurement of other types of coatings, both metallic and non-metallic.

Keywords: industrial on-line XRF analysis, X-ray coating thickness analyzer, industrial coating quality control and monitoring, phosphate coatings on rolled steel.

1. Introduction

Phosphating is the most widely used process for surface treatment and finishing of both ferrous and non-ferrous metals. Because of its economy, speed of application and its ability to provide excellent corrosion and wear resistance, adhesion and lubrication properties, phosphating plays a significant role in the automobile, process and appliance industries. Changes in the end use of phosphated articles have resulted in the development of innovative production methods designed to achieve the desired coating properties. Narayanan published a review of this new technology and the associated analytical techniques used to develop and monitor the processes [1]. Zimmermann *et al.* used X-ray fluorescence (XRF) and scanning electron microscopy (SEM) to monitor the nucleation and growth rate of Ni^{2+} coatings of Zn-Ni alloys in new phosphating processes [2]. Now, new accelerators such as silica nano particles are being introduced to improve the performance of phosphate coatings against corrosion [3].

Phosphate coatings consist of a fine, crystalline film that contains insoluble iron phosphates together with manganese or zinc phosphates. After proper treatment with oils, varnishes or paints, phosphate coatings reliably protect the metal from corrosion. Phosphate-zinc coatings are usually applied with a thin 1–3 μm thick layer, which corresponds to a coating surface gravity of 1.0–3.3 g/m^2. Phosphate-iron coatings are used less often. Their thickness is normally 0.3–0.8 μm [4,5]. In addition to

DOI: https://doi.org/10.26799/cp-surfcoatkorea2018

corrosion protection, phosphate coatings are widely used for electrical insulation, to reduce friction and as a primer for paint and varnish coatings. The essence of the process of precipitation of phosphate coatings is the treatment (immersion or spraying) of the metal surface with acidified solutions of mono substituted phosphates. As a result, a film of insoluble phosphates forms on the surface.

Measuring the thickness of coatings is a challenge for both the finishers and the companies that receive finished components. Defective coatings lead to the formation of rust and other defects on the surface of the material. The coating process usually involves selective quality control (random sampling): measurements are performed by the operator at line with portable analysers or random samples are delivered to a laboratory. Typically, portable X-ray fluorescence gauges or gauges based on eddy-current, magnetic induction and Beta-backscatter are used for this purpose.

In recent years, manufacturing engineers have recognized the importance of automatic quality control procedures for monitoring coating thicknesses that can provide them with continuous, real-time data. These data are automatically measured and stored electronically in a plant database. It is easy to retrieve and use the necessary information in case of possible claims. Testing the coating thicknesses online means increased productivity and improved process efficiency and eliminates over-coating or under-coating of the finished goods.

Accurate thickness measurements depend on the design characteristics of the analyser and how well they are met. State-of-the-art instrumentation, along with the computer hardware and software packages now available with X-ray fluorescence systems, has significantly reduced inspection time and improved accuracy, repeatability and reproducibility. In addition, online quality control does not require cutting the sample (cutting a metal strip to cut out subsamples with subsequent removal of the coating and weighing of coated and uncoated samples), thus decreasing labour cost and intensity.

The publications on the industrial application of online X-ray coating thickness analysers, which were found in the research literature and industrial journals, are limited to laboratory table-top or hand held instruments [6-8]. AXIC Application Report No.1 describes the results of a laboratory analysis of the phosphorus content of silicate glasses on silicon substrates and their thicknesses. Measurements were performed in a fabrication environment with the AXIC-100 XRF system [9]. The range of glass film thicknesses described in this application report was from 30 to 3000 nm.

No articles on real-time measurement of phosphate coating thickness on a moving steel strip with the help of industrial online XRF instrumentation were found. The lack of publications on industrial applications of online XRF analysers can be explained either by a serious underestimation of the potential demand for such measurements or by the complexity of such a projects and long time required to implement it.

2. Principles of XRF Coating Measurements and Description of the Instrument

Energy dispersive X-ray fluorescence analysis (ED-XRFA) can be used to qualitatively and quantitatively determine the elemental composition, as well as the thickness of single- or multi-layer coatings applied to substrates. The XRF method works non-destructively and without making contact with the surface. Measurements can be performed quickly and usually do not require careful sample preparation.

The principle used in XRF instruments is the following: an X-ray tube (1) irradiates by primary XRF excitation (2) the surface (3) of the material under test (Fig.1a, b). Secondary X-ray fluorescence (4) is generated both in the substrate and any potential coatings on its surface. A detector (5) counts incoming X-ray photons and measures their energies. The X-ray fluorescence spectrum is recorded and analysed by means of a spectrometer (6). The intensity of one of the fluorescence lines emitted by the coating or substrate is used to calculate the coating thickness by PC (7). The film thickness can be determined in one of two ways, depending on the substrate composition: either by emission of characteristic X-rays emitted by the film of interest, or by absorption of the characteristic X-rays of the substrate by the coating itself (Fig. 1a). In the case of phosphate coatings, the thickness of the phosphate film can be obtained from the intensity of the phosphorus K-line generated by the coating itself.

With the **emission method,** the element in the film that is being used to determine the thickness should be absent in the substrate. An uncoated sample of steel was checked for traces of phosphorus before the calibration. It was shown that the phosphorus line was not identified in uncoated samples under the measurement conditions.

1. Features of the CTA-02 Design

The design of developed industrial XRF coating thickness analyzer CTA-02 schematically presented on Fig.2. Analyzer consists of two XRF gauges, mounted above and below the steel strip and capable of moving across the

DOI: https://doi.org/10.26799/cp-surfcoatkorea2018

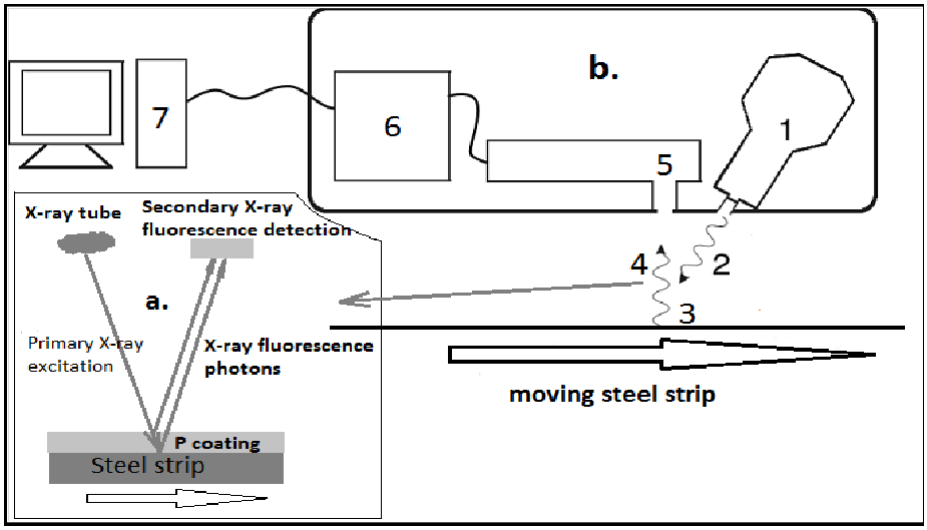

Fig.1. XRF emission of a phosphorus fluorescence line from a phosphate coating on a steel substrate (a) and schematic diagram of an XRF on-line coating thickness analyser (b)

moving strip, construction system for their suspension and relocation and electronic control unit. XRF gauge for the analyser is designed and manufactured on the basis of CON-X analyser (Fig.3), which is serially produced for XRF elemental analysis [10,11]. Basically, it is a classic design of XRF equipment, but in case of CTA-02 it is specially modified and customized to suit the requirements of the application and the industrial environment.

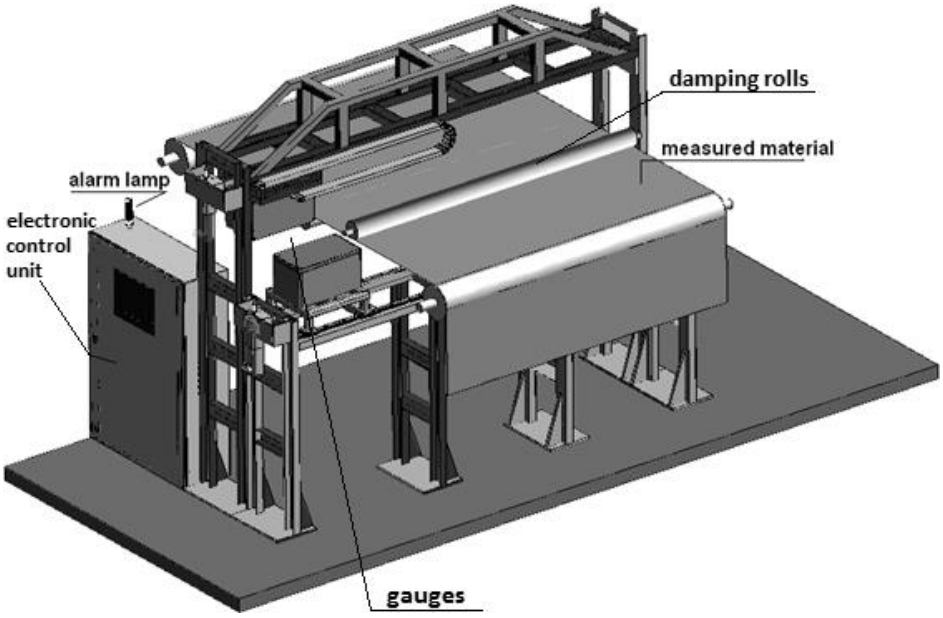

Fig.2. Schematic view of the CTA-2 installation on the end-user production line

DOI: https://doi.org/10.26799/cp-surfcoatkorea2018

Accurate online coating thickness analysis is possible only if the results are not affected by variations in external parameters, such as the distance between the material surface and the measuring head, temperature and humidity of the material and industrial environment, surface uniformity and smoothness, etc. A number of particular features of the analyser's intended application required the design of modifications and novelties to the series-production CTA. These requirements were realized in CTA-02 and they are as follows:

1) The thickness of a light non-metallic coating (phosphate salts) on a metal substrate (steel) shall be measured.

2) The analyser shall be provided with a special measuring gauge that is held close to the surface (4 mm between the surface of the material and the measuring unit) and a specially designed line shall supply helium to the measuring space. The reason is that a phosphorus XRF line (P Kα) was chosen for the measurements. The fluorescence yield of P Kα is rather low (Z =15). In order to increase the sensitivity of XRF to elements with low atomic numbers (such as Mg, Al, Si, P and S), XRF measurements should be made in close proximity to the surface of the coating and preferably in a Helium atmosphere to prevent the absorption of P fluorescence by atmospheric Argon.

3) When He flushing is used, the pressure and flow rate of the Helium shall be very stable so as to avoid fluctuations in the results. A specially designed measuring head with a built-in Helium supply line is used to provide a stable flow of Helium.

4) The thickness of the rolled steel strip varies from roll to roll. The distance between the measuring block and the measured material is extremely critical for accuracy of the results. That is why the CTA-02 is provided with specially designed, movable measuring head capable of maintaining a constant distance between the measuring block and the measured material. The distance from the measuring head to the metal strip is controlled and adjusted with the help of a motorized vertical lift stage. It provides precise vertical movement control for lifting or lowering the XRF measuring unit. The stage is equipped with a stepper motor. It is controlled by special controller board that communicates with the embedded microprocessor of the CTA-02.

A special optoelectronic displacement sensor is integrated in the measuring system to account for changes in the distance between the analyser and the steel strip surface. It is used to determine optically the distance to the object and is very sensitive to distance changes. The sensor's controller board also communicates with the embedded microprocessor and transmits data about the distance to the steel strip. The sensor is mounted at the bottom of the side frame of the analyser in close vicinity to the strip being measured (Fig.3).

Fig.3. XRF gauge of CTA-02 analyser with optoelectronic displacement sensor (at the bottom of the frame on the right)

5) To ensure optimum conditions for the excitation of the P Kα line, the parameters of the primary X-ray excitation and the design of the tube itself were carefully selected. A low-voltage X-ray tube provides stable primary excitation parameters (low anode voltage and high anode current). The low anode voltage and high current provide the optimal conditions for excitation of the P Kα line, thus ensuring maximal fluorescence yield of the phosphorus line.

6) The fluorescence line from the coating shall not to be too close in energy to any of the fluorescence lines of the substrate. A high-resolution SDD shall be used in the measuring unit.

DOI: https://doi.org/10.26799/cp-surfcoatkorea2018

7) The high ambient temperatures found in the site of operation require the use of Vortex adiabatic coolers in order to protect the internal components of the analyser from overheating and provide thermo-stabilization inside the measuring box. Vortex technology shall maintain the internal temperature within the specified range (below 40°C).

2. Calibration of the Coating Thickness Analyser

In-house laboratory calibration of the CTA-02 was carried out using calibration samples that covered the range of thicknesses of phosphate film to be measured. Calibration samples were provided by the customer. An example of a calibration sample is shown in Fig. 4.

Assuming that the film density and composition does not change, it is possible to determine the thickness of the phosphate coating by measuring the intensity of the emission of the P Kα XRF line. If one of the parameters changes, it is desirable to have an appropriate set of calibration samples and to carry out an individual calibration for each grade of product.

The measurement conditions for the XRF calibration spectra were as follows: X-ray tube anode material: Mo; X-ray tube voltage and current: 7.5 kV and 1900 μA; measurement time: 30 s**;** distance between the sample and analyser bottom: 4 mm.

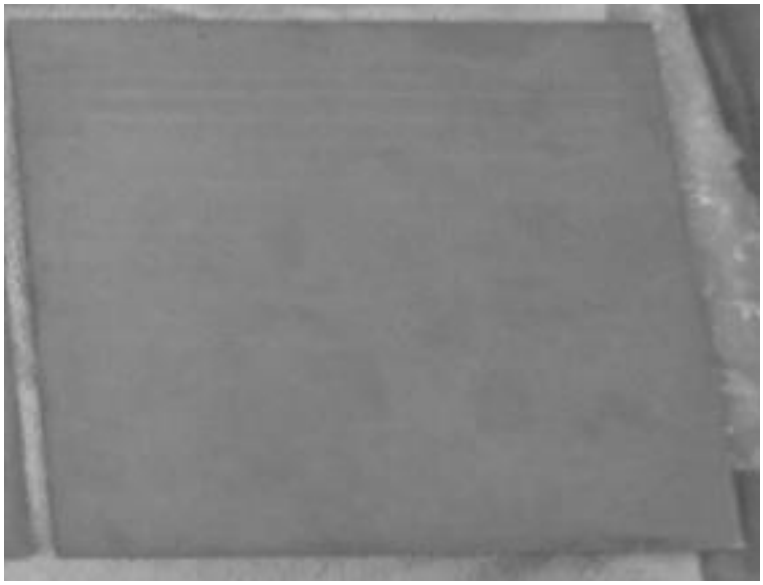

Fig.4. Appearance of a phosphate coating on steel

XRF spectra of two calibration samples measured at preset values of the X-ray tube excitation parameters are shown in Fig. 5 as an example. The spectra were measured both in air and using the Helium purge of the measuring space. Helium was used to displace part of the air from the measuring space, which improved the conditions for the excitation and detection of phosphorus line. The CTA-02 is equipped with a specially designed helium purge system that provides a constant flow and concentration of helium in the measuring space. From Fig. 5 it can be seen that the intensity of the phosphorus line grows proportionally to the coating thickness. What is more, in a helium atmosphere, the intensity of the P Kα line is higher than in air and rises with thickness growth more rapidly.

As a calibration parameter we used the ratio of the intensity of the P Kα XRF line to the intensity of Mo Lα line of the X-ray tube. On the calibration plot (Fig. 6) line intensities are denoted as P Spb and Mo-L Spb. The ratios approach was used to compensate for small deviations in the measurement conditions (deviation in distance between sample surface and measuring unit or small changes in the helium flow rate) and in spectral statistics.

DOI: https://doi.org/10.26799/cp-surfcoatkorea2018

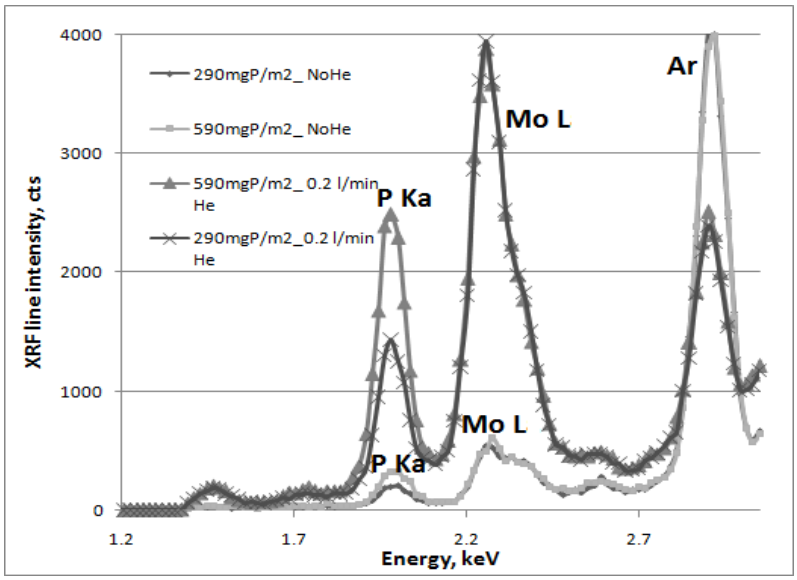

Fig.5. XRF spectra of phosphate coated calibration samples. Parameters of the measurement: X-ray tube anode material: Mo; X-ray tube voltage and current: 7.5 kV and 1900 µA; measurement time: 30 s**;** distance between the sample and analyser bottom: 4 mm. The Mo-L lines have an instrumental origin. The Ar Kα line is generated in the air between the analyser and the sample surface.

The calibration curve is shown in Figure 6. The ratio of the intensities of the P Kα and the Mo Lα lines is plotted relative to the thickness of the phosphate coating. The parameter (P Kα Spb/Mo-L Spb) is proportional to the thickness, but displays a kind of "saturation" phenomenon (Fig. 6). This behaviour has two main causes: self-absorption of the P Kα line in the measured layer [12] and peak pileup [13]. These two phenomena lead to a nonlinear response curve that can be fitted to a good approximation with a second-order polynomial curve, $T = aI^2 + bI + c$, where T is the thickness of the deposited layer, and I is the ratio of the intensities of the P Kα and Mo-L fluorescence peaks. The intensities are automatically calculated by the program according to a widely known empirical approach to the selection of the region of interest (ROI), which has been described by Carapelle *et al.* [5]. The coefficients *a*, *b*, and *c* are calculated by a program using a classical fitting procedure.

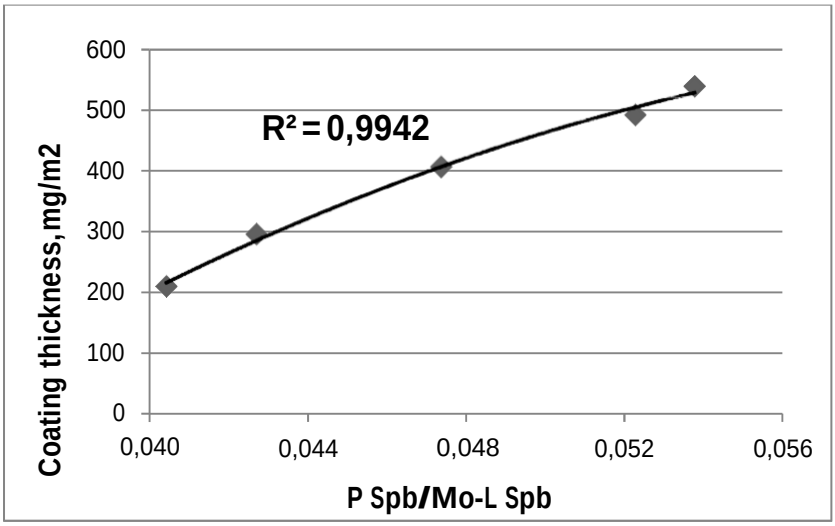

Fig.6. Calibration curve of the phosphate coating thickness on steel. The calibration paramenter is the ratio of the intensities of the P Kα and Mo Lα XRF lines, which is plotted on the horizontal axis, while the thickness of the coating is plotted on the vertical axis. The correlation coefficient R^2 is close to 1.

DOI: https://doi.org/10.26799/cp-surfcoatkorea2018

The use of the least squares method showed that the polynomial function of second order is the most suitable: the correlation coefficient R^2 of the best fit is close to 1, which indicates that the calibration parameters are strongly and positively correlated via a polynomial relationship.

3. Helium flow test

The dependence of the P Kα, Mo-L, and Ar Kα XRF line intensities on the helium flow rate is shown in Fig. 7. As expected, the He purge improves the spectral statistics of the P Kα XRF line. At a helium flow rate of about 0.25 l/min the intensity of the P XRF line increases by 3–4 times compared to air. The intensity rises substantially up to a flow rate of 0.5 l/min. Further increases in the helium flow rates lead to the establishment of a dynamic equilibrium in the gas mixture within the measuring space. As a result, the intensity of the phosphorus line almost stops increasing.

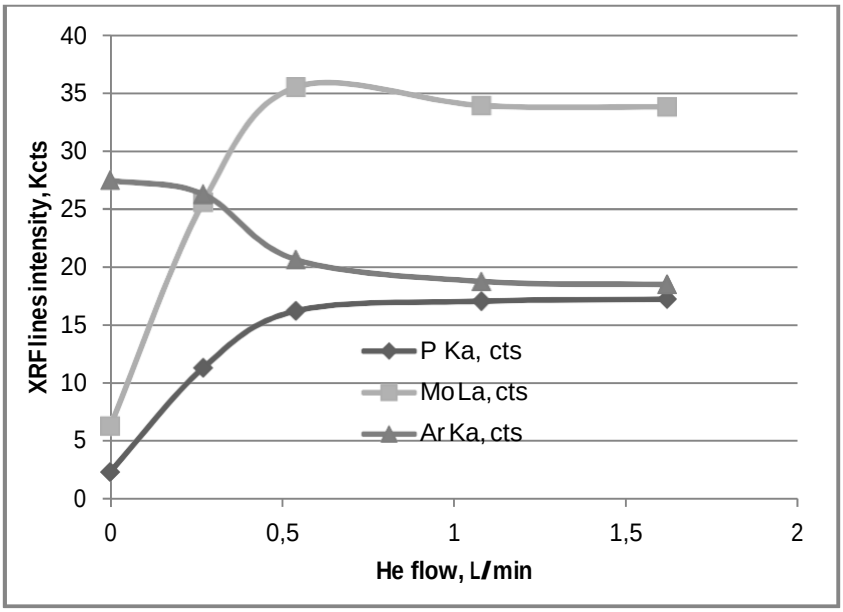

Fig.7. P Kα, Mo-L (X-ray tube) and Ar Kα (from air) line intensities are shown as a function of the helium flow rate.

The test with helium flow was carried out in static laboratory conditions (samples were maintained at a fixed position). The vortex coolers were disabled during this test. The following statistical parameters of the P Kα XRF line were estimated for a measurement time of 10s (Table 1) at different helium flow rates: detection limit (DL), absolute statistic accuracy (sigma) and relative accuracy (sigma relative).

Table 1 shows that the DL estimated for static laboratory conditions is ~3 times lower and the accuracy ~3 times higher in the helium atmosphere than in air. This results confirm that the design of the helium supply that is used in the CTA-02 analyser works efficiently: it provides a dynamic flow and a stable concentration of helium in the space between the measuring head and the material, which improves the analytical parameters used to determine the thickness of the phosphate coating.

DOI: https://doi.org/10.26799/cp-surfcoatkorea2018

Table 1. Statistical parameters for the P Kα XRF line (P in the phosphate coating on steel) calculated for measurements in air and at different helium flow rates. (Spb - gross area (intensity) of XRF spectral line, S_p and S_b - net and background areas (intensities) of XRF spectral line, cts – counts - number of photon detected in spectral line).

Helium flow, L/min	P Kα XRF line statistical parameters, time = 10s					
	P Kα Spb, cts	P Kα Sp, cts	P Kα Sb, cts	DL, mg P/m^2	sigma, mg P/m^2	sigma, rel %
0	2381	1571	810	32	42	1.78
0.27	11323	7903	3420	13	18	0.16
0.54	16232	11162	5070	11	15	0.10
1.08	17069	11857	5212	11	15	0.09
1.62	17245	12558	4687	10	14	0.08

4. Software

The dedicated software **ThMeter** is designed for automatic and continuous (24/7) control of two CTA-02 coating thickness analysers, scanning both sides of steel strip, developing and testing methods for measuring the thickness of new coatings and storing measurement results offline and retrieving them for viewing. The program calculates the current values of the coating thickness, continuously monitors the state of the spectrometers, X-ray tubes and detectors, restores the operating modes in case of equipment failure during the measurement mode, automatically carries out calibration runs when creating a new measurement method, and exchanges data with the computer located in the control room. All data on the current measurements, the operation and calibration modes, the status of all spectrometric equipment, including the state of the X-ray tubes and detectors, are transmitted to the computer in the control room, and commands are received from there to control the analyser's movements. All data are transmitted in the JavaScript Object Notation (JSON) text file format.

5. Pre-acceptance test and Factory Acceptance Test. Results and discussion

During the **Pre-Acceptance Test (PAT)** more than 50 control samples of phosphate coatings on steel were tested using pre-calibrated XRF gauges in the XRF applications laboratory of Baltic Scientific Instruments with the participation of the end user. The end user provided these control samples with known thicknesses of the phosphate film. The values measured with the CTA-02 analyzer were compared to the control values. The accuracy of the cross-check was determined in terms of the root mean square deviation (RMSD) calculated for the entire set of control samples (n=50). The majority of the values measured during the PAT fell within ± 10% relative error, which meets the requirements of the end user.

The CTA-02 measurements from the cross-check are plotted together with the control reference values in Fig.8. Differences between the control reference values and thicknesses determined by the CTA-02 analyzer are small and fall within the end user's requirements.

DOI: https://doi.org/10.26799/cp-surfcoatkorea2018

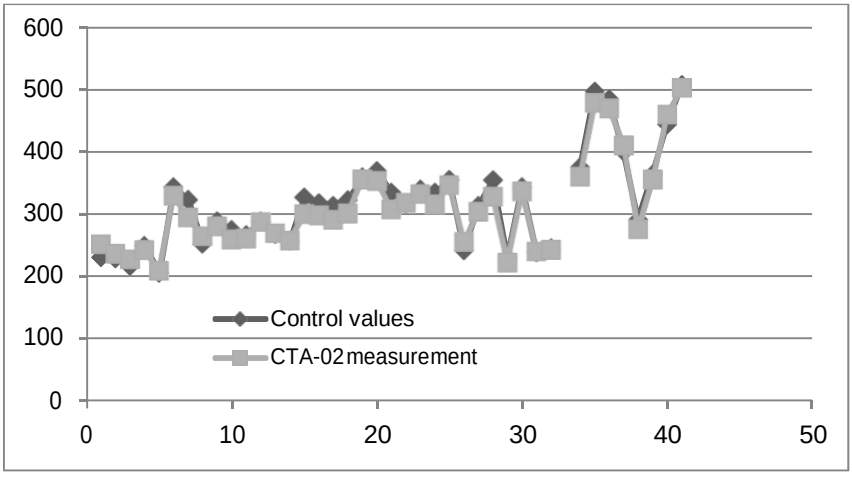

Fig.8. PAT cross-check of CTA-02 measurements together with control reference values

A **Factory Acceptance Test (FAT)** of the CTA-02 analyzer operation was performed during full-scale operation in the following way. Two XRF gauges were attached to suspension and relocation frames mounted on rails that allow the gauges to move across a continuously moving steel strip. The analyser consists of two gauges, one mounted above, and the other below, the steel strip. The gauges take into account the synchronisation between the movements of the strip and the measuring head, while changes in distance or thickness of the steel strip are checked by the embedded displacement sensor and are automatically compensated. Analysis can be performed in either 'skating mode' or step-by-step mode, revealing the distribution of coating thickness across the entire width of the strip. Coating thickness analysis of one measured step-by-step band can be available in just 10 seconds, depending on the application.

The CTA-02 analyzer is provided with a self-contained automatic calibration device. The device is equipped with a specially designed sample holder. Both gauges can be commanded from the control room to move along the rails to a specially configured calibration space away from the production line.

The average phosphate thicknesses for rolls of coated steel, measured by the CTA-02 analyzer, were compared to laboratory results of random control samples. The comparison was carried out during 3 days of continuous operation of the production line. The measurement accuracy shown during long-run factory acceptance test was 10–15%.

6. Conclusions

The capabilities of the CTA-02 analyzer for continuously and automatically analysing the thickness of phosphate coatings of moving strips of rolled steel during production was demonstrated during the PAT and long-term Factory Acceptance Test in full-scale operation at a large steel plant. The CTA-02 analyzer showed stable operation and provided process engineers with reliable results in real time during the entire duration of the tests. The measurement accuracy shown during long-run factory acceptance test was 10–15%. In summary, the CTA-02 XRF coating thickness analyzer can meet the needs of general metal finishers, who are concerned with corrosion resistance and wear resistance, as well as the automotive industry with its need for analysis of coating passivation or the aerospace industry, which has the added concern of corrosion resistance and lubricity at high temperatures.

DOI: https://doi.org/10.26799/cp-surfcoatkorea2018

7. References

1. T. Narayanan. Rev. Adv. Mater. Sci., 2005, 9(2), 130–177.

2. D. Zimmermann, A.G. Munoz, J. W. Schultze. Surf. Coat. Technol., 2005, 197(2–3), 260–269.

3. M.O.W. Richardson, R.E. Shaw. In book: Corrosion, 1994, pp.15:22-14:37, DOI 10.1016/B978-0-08-052351-4.50119-9.

4. Australian Standard No. 1627.6-1977. Phosphate Treatment of Iron and Steel Surfaces.

5. Tables of phosphate coating thicknesses: http://www.kiesow.org/en/products/phosphating-processes/

6. M. Salmi, A.Magrini, G.Gigante, O.Barra. Coating Thickness Measurement by Means of the Radioisotope X-Ray Fluorescence Technique. Isotopen praxis, 14, 380-381, 1978.

7. A.Carapelle, K.Fleury-Frenette, J-P.Collette. Portable XRF spectrometer for coating thickness measurements, Review of Scientific Measurements, 2007, v.78, issue 12.

8. A.Carapelle, J-M. Defise, D. Strivay, H-P.Garnir. Handheld modern computer brings new features to portable X-ray fluorescence coating thickness measurement device. Computer Physics Communications, 2011, 182, 1304-1306.

9. AXIC Application Report No. 1, Analysis of Phosphorus in PSG and BPSG with the AXIC-100 XRF System, 1988

10. A.Sokolov, D.Docenko, E.Bliakher, O.Shirokobrod, J.Koskinen. On-line analysis of chrome–iron ores on a conveyor belt using x-ray fluorescence analysis. X-Ray Spectrometry, 2005; 34, pp. 456–459.

11. http://bsi.lv/en/products/xrf-analyzers/-line-xrf-conveyor-analyzer-con-x/

12. R. E. Van Grieken and A. A. Markowicsz, *Handbook of X-Ray Spectrometry*, Practical Spectroscopy Series Vol. 29, 2nd ed. Dekker, New York, 2002 p. 366.

13. R. E. Van Grieken and A. A. Markowicsz, *Handbook of X-Ray Spectrometry*, Practical Spectroscopy Series Vol. 29, 2nd ed. Dekker, New York, 2002, p. 243.

Proceedings of SurfCoat Korea 2018 International Conference
Incheon, Rep. Of Korean, March 28 - 30, 2018
DOI: https://doi.org/10.26799/cp-surfcoatkorea2018

Graphite Raman vibrations as a probe of thermal degradation in hydrophobic graphite-based thin film coatings

Vanessa Gutiérrez-Cano[1], Jesús A. González[1], Vanesa Díaz[2], Fernando Rodríguez[1]
[1] DCITIMAC, Sciences Faculty, University of Cantabria
Avda. los Castros S/N, 39005, Santander, Spain, gcanov@unican.es
[2] BSH Electrodomésticos España, S.A.,
Eduardo García 30, 39011, Santander, Spain

Abstract
In this work, we present an alternative method to characterize thermal coating degradation of graphite-based thin-film coatings. Raman experiments show that D and G vibrational modes of graphite are a powerful probe for determining the degradation of graphite-based coatings. The degradation temperature of the coating was correlated with anomalies exhibited by the temperature dependence of the G and D modes. Contact angle measurements and thermogravimetric analysis support Raman results confirming the method feasibility.

Keywords: Raman spectroscopy; carbon-based materials; graphite; thermal degradation; hydrophobic coatings; contact angle.

1. Introduction

Hydrophobic and superhydrophobic coatings have recently attracted scientific and technological interest due to their wide range of applications. Since the Lotus leaf structure was first discovered by Barthlott and Neinhuis in 1997 [1, 2], lots of materials have been developed on the basis of the micro- and nano-structures of this system. There is an ample variety of applications of hydrophobic and superhydrophobic surfaces. Optical devices [3, 4], self-cleaning coatings for window glasses and solar panels [5, 6], paints and varnishes [7], anti-corrosive coatings [8, 9], anti-icing layers and non-wetting fabrics [10, 11] are examples of remarkable applications. However, all these materials are based on the sample principle requiring micro/nano-roughness and low surface energy [12-14].
In order to achieve these two requirements, the addition of nanoparticles to some organosilane matrix is the most commonly explored synthesis route [15, 16]. The addition of carbon-based materials is of great interest because of their low-density, high surface roughness and non-polar nature [17-21]. Particularly, graphite and graphene oxide are high temperature resistant materials, with a good capability to get mixed with other materials, thermal shock and oxidation resistant and a flexibility [22].
Depending on the coating application, some properties like thermal resistance, hardness or adherence are important to find novel coatings. So far, only a few studies have been carried out to determine coated surface degradation as a result of a thermal treatment, except for the widely used contact angle measurement technique [23].
In this work, we present Raman spectroscopy as an alternative method to determine thermal coating degradation. Raman measurements show that both D and G vibrational modes of graphite are efficient probes for determining the temperature degradation of graphite-based coatings. Spectroscopic results are consistent with contact angle (C.A.) measurements and thermogravimetric analysis supporting method feasibility.

2. Experimental

2.1. Materials

304 stainless steel (SSL) grinded foils were used as a substrate. A hydrophobic ceramic-based coating (average thickness < 1 μm) was sprayed onto the metallic surface with an aerosol. Nano-graphite inclusions were incorporated by spray before curing, following a similar procedure described elsewhere [21]. The presence of the nano-graphite inclusions was clearly corroborated through characteristic G and D peaks by Raman spectroscopy with laser focusing in the as-prepared nano-coating.

2.1. Methods

2.2.1. Raman Spectroscopy

Raman spectra were acquired with a Horiba T64000 Raman spectrometer equipped with a triple monochromator in the subtractive configuration (spectral resolution of 0.6 cm^{-1}), coupled to a confocal microscope. The 514.5 nm line of a Coherent Innova Spectrum 70C Ar^+- Kr^+ laser was used as the excitation source. A liquid-nitrogen-cooled CCD Jobin-Yvon Symphony was used as detector. Temperature-dependent measurements in the 25-500 ºC range were carried out in a 1x1 cm^2 sample of coated SSL using a heating stage Linkam TS1000, with a 20× objective and a laser power on sample below 5 mW. Spectra were acquired 10 min. after varying the temperature to achieve thermal stability. Spectra were taken in the same point of the sample to avoid differences in the spectral shape because of coating micro-inhomogeneities.

2.2.2. Hydrophobicity measurements: contact angle (C.A.)

Hydrophobicity of the coating was determined by measuring the static C.A. angle of distilled (DI) water using a Mobile Surface Analyzer – MSA from Kruss. The shape of 1 µl sessile drops of DI water was measured. Reported values were calculated by taking the average of 6 different measurements per sample, following random directions of the grinding to minimize the influence of the roughness direction.

2.2.3. Thermogravimetry and mass spectrometry (TG-MS)

Simultaneous TG-MS measurements were carried out with a SETARAM thermal analyser SETSYS-1700. Two samples of 1x1 mm^2 of coated SSL were placed in a platinum crucible in an air atmosphere and heated from 25 to 550 ºC at a heating rate of 0.5 ºC/min. The TG instrument was coupled to a Balzers Thermostar/Omnistar QMS 200 mass spectrometer for evolved gas analysis. The selected m/z signal was 43.94 (CO_2^+).

3. Results and discussion

Thermal degradation of the coating was determined by Raman spectroscopy by studying the variations of D and G graphite vibrational peaks. The obtained results correlate with C.A. measurements and thermogravimetric and mass spectrometry experiments.

3.1. Raman spectroscopic analysis of the coating

Figure 1 shows the Raman spectra of the coating as a function of temperature. The more intense peaks of the spectra are associated to the so-called D and G vibrational modes of graphite. These peaks are located at 1355 and 1581 cm^{-1}, respectively, and its presence in the Raman spectra confirm the incorporation of the nano-graphite inclusions in the coating matrix.

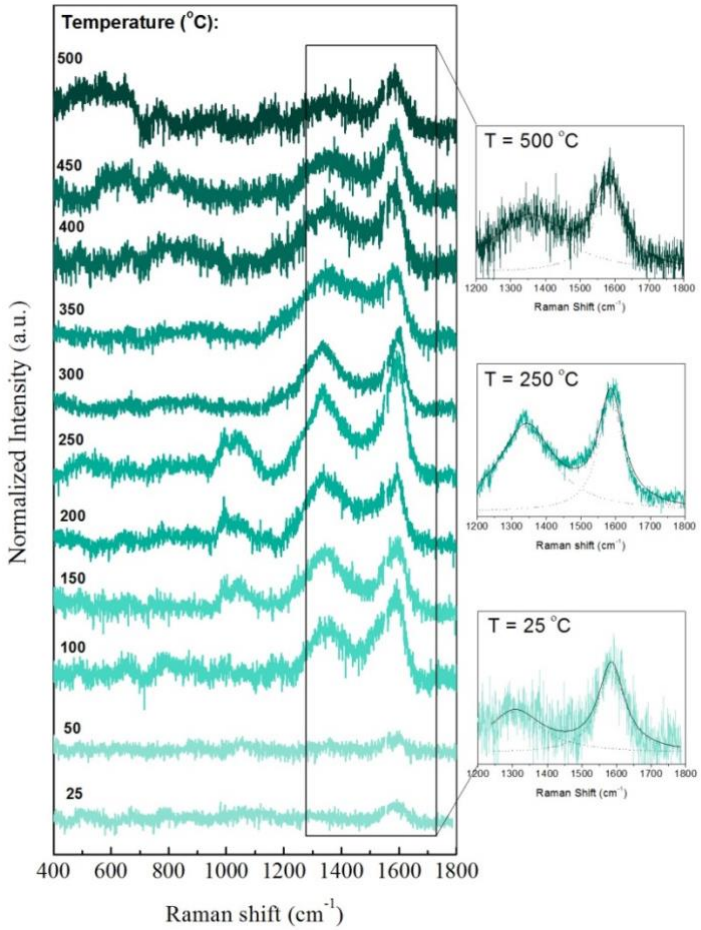

Fig. 1: Raman spectra of the coated stainless-steel sample at different temperatures. The laser excitation wavelength was λ=514.5 nm and the light power on sample was 5 mW.

Interestingly, the profile analysis of the G and D vibrational peaks unveils the presence of disordered carbon. On the one hand, the G mode, located at 1581 cm^{-1}, has E_{2g} symmetry and it is associated to bond-stretching motion of sp^2 C-C pairs. It can be found in the range 1500-1630 cm^{-1} depending on the sample matrix, pressure and temperature conditions [24]. On the other hand, the D mode, located at 1355 cm^{-1}, has A_{1g} symmetry and is associated with a breathing mode of sp^2 atoms forming hexagonal rings. Its broadening and intensity are both strongly related to the particle size of the graphitic regions limited by adsorbed-atom defects yielding disordered graphite. The smaller the crystallite, the more disordered the graphite. The nanometric size of these small crystallites (Lα) is given by the empirical relation [25]:

$$L\alpha\ (\mathrm{nm}) = \frac{1000}{227\ (I_D / I_G)} \tag{1}$$

where I_D and I_G correspond to the intensities of D and G vibrational peaks, respectively.

The line-shape analysis of these two bands provides the frequency, band width (FWHM), intensity, and hence the D-to-G intensity ratio. On the one hand, the broader the band, the higher the disorder. The Raman spectra of Fig. 1 show that the D-band intensity is higher than the G-band intensity reflecting a small value Lα, thus, more defects in the graphite [26]. As it is shown in Fig. 2A, D band undergoes an abrupt shift of 30 cm^{-1} at about 350 ºC. This phenomenon is also reflected through the variation of Lα; the D-to-G intensity ratio is also sensitive to these changes in the coating matrix, as it can be seen in Fig. 2B. The graphite disorder, evidenced by the sp^2 cluster size of graphite (Lα), passes through two minima (maximum disorder) at 200 and 350 ºC indicating the formation of sp^3 bonding, due to oxidation processes. These two magnitudes are a probe of the thermal degradation of the coating, as it will be demonstrated below.

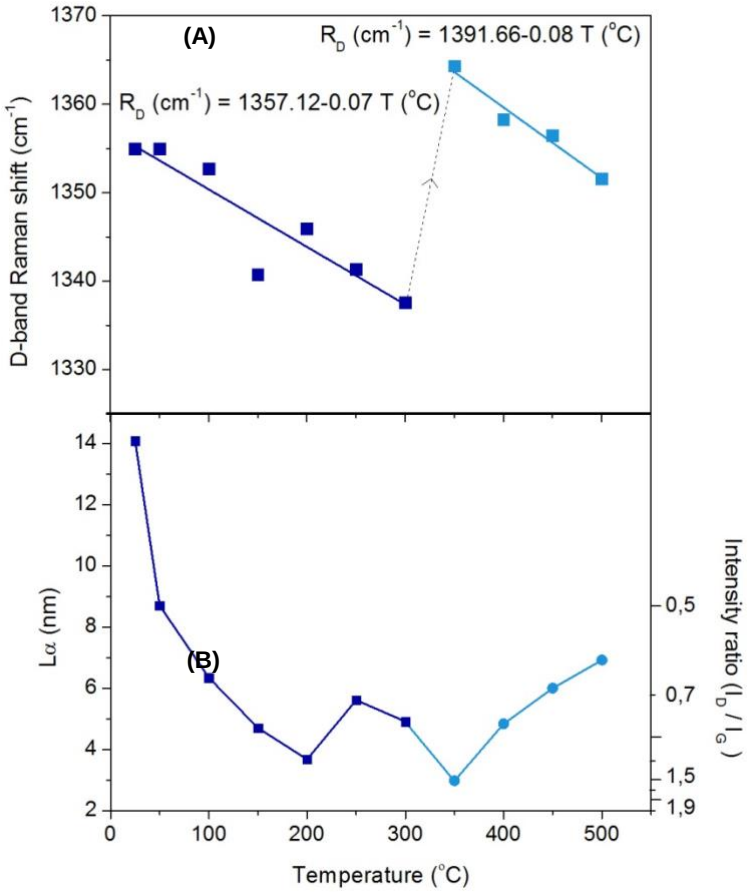

Fig. 2: Spectroscopic data: (A) Temperature dependence of the Raman shift of graphite's D-band. (B) Temperature dependence of the graphite sp^2 cluster size (Lα).

3.2. Hydrophobicity and thermogravimetric analysis

The coating wettability was analysed through the measurement of static DI water C.A. on the coating. Table 1 includes the C.A. values as a function of the annealing temperature of the coated sample; these values are represented in fig. 3A. The coating shows a hydrophobic behaviour at room temperature (C.A. = 95º). Nevertheless, its properties become degraded when the sample is exposed to higher temperatures and consequently the C.A. decreases. The coating loses its hydrophobic character when the annealing temperature is around 200 ºC. However, at higher temperatures (350-400 ºC) the properties become highly degraded. The C.A. decreases to 25 ºC and the wettability of the surface is complete, the coating becoming totally hydrophilic [27].

Table 1: Hydrophobicity of the coating: contact angle (C.A.) values as a function of the temperature (T). All samples were annealed for 1 h in a stove. C.A. values were calculated by taking the average of 6 different measurements on each sample following random directions.

T (ºC)	C.A. (º) DI water
25	95
50	92.5
100	90.5
150	93.1
200	91.2
250	80.5
300	72.6
350	72.0
400	27.0
450	23.2

500	25.6

In order to understand the nature of this degradation, we performed thermogravimetric and mass spectrometry measurements. Figure 3B shows the TG-MS results in the 25-550 ºC range. It must be noticed that mass (in black) and emission (in green) variations have small relative values because the samples introduced in the crucible were remarkably small (10^{-3} mm^3). As it can be seen in the spectrum, there are two significant mass loses at 200 and 350 ºC. Additionally, the MS signal shows a significant CO_2 emission at 200 ºC. On the one hand, the degradation step at 200 ºC is explained by the condensation of carboxyl and hydroxyl groups of the coating [28]. On the other hand, the degradation step involving other functional groups occurs occurring at 350 ºC and at higher temperatures because of oxidation of graphite groups in the coating matrix. These groups act as heat-transport retarders by slowing the out-diffusion and migration of volatile molecules from the matrix to the surface of the coating [29].

These results are in good agreement with the measured values of hydrophobicity but also with the Raman spectroscopy ones. The C.A. shows a singular behaviour between 200 and 350 °C, and abruptly decreases after 350 °C. Similarly, the graphite Raman D band experiences a slight redshift between 200 and 350 °C, followed by an important blueshift (Fig. 2A), which is also accompanied by an anomalous variation of the sp^2 cluster size (Lα) between 200 and 350 °C, with Lα varying between 3 and 6 nm up to 500 °C (Fig. 2B).

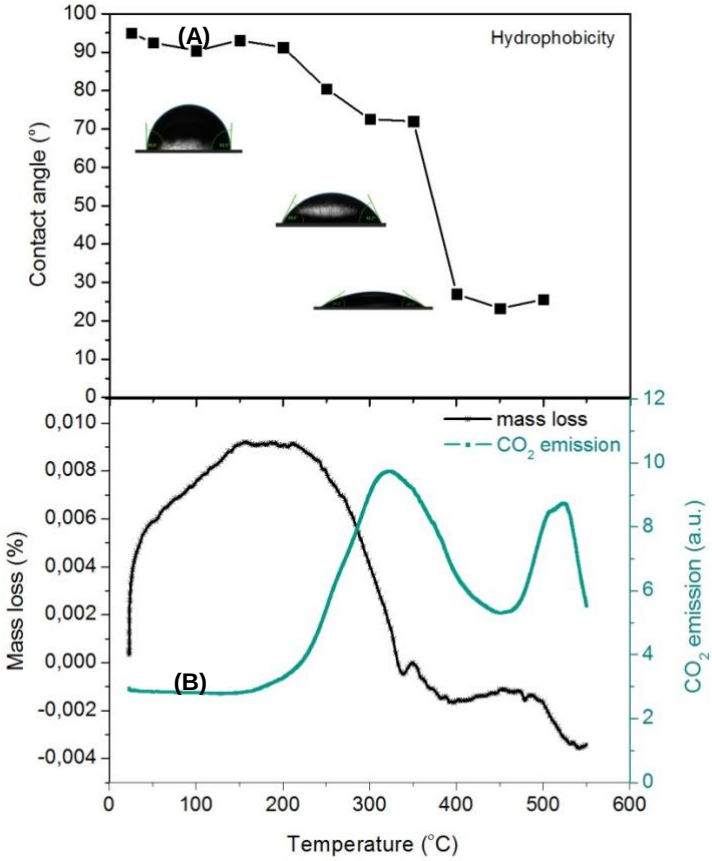

Fig. 3: (A) TG-MS spectra of coated samples in air. TG curve is shown in black and MS curve of CO_2^+ is presented in green. (B) Hydrophobicity measurement of the coating: water contact angles as a function of the thermal treatment.

4. Conclusion

In this work we demonstrate that the Raman vibrations of graphite, the so-called D and G modes, are efficient probes to characterize the coating degradation as consequence of thermal treatments. Both D-band shift and sp^2 cluster size show anomalies in their variation with the annealing temperature. This effect was similarly observed in TG-Ms and hydrophobicity measurements, the measurements of which were carried out in parallel to the Raman measurements. We conclude that thermal coating degradation correlates with the loss of volatile species of the coating that occurs in parallel to the degradation of the coating-incorporated graphite. Indeed, graphite acts as a trap of these volatile species thus preserving the hydrophobic character of the coating. It completely disappears above 350 ºC.

Acknowledgements

This work has been supported by B.S.H. Electrodomésticos España, S.A. V. Gutiérrez thanks BSH for a research grant. The authors want to thank Prof. F. González from the Inorganic Chemistry Department, University of Cantabria, for his collaboration in the TG-MS measurements.

References

1. W. Barthlott and C. Neinhuis, "Purity of the sacred lotus, or escape from contamination in biological surfaces", Planta, vol. 202, no 1, pp. 1-8, 1997.
2. C. Neinhuis and W. Barthlott, "Characterization and distribution of water-repellent, selfcleaning plant surfaces", Ann. Bot-London, vol. 79, no 6, pp.667-677, 1997.
3. M. Popall, J. Schulz, B.-E. Olsowski, A. Martin and K. Bühler, "Hydrophobic coating for ink jet printing heads", US Patent 6 283 578, Sep. 4, 2001.
4. X. Zhang, X. Liu, J. Laakso, E. Levänen and T. Mäntylä, "Easy-to-clean property and durability of superhydrophobic flaky γ-alumina coating on stainless steel in field test at a paper machine", Appl. Surf. Sci., vol. 258, no 7, pp. 3102–3108, 2012.
5. J.-H. Shin, K.-S. Han and H. Lee, "Anti-reflection and hydrophobic characteristics of M-PDMS based moth-eye nano-patterns on protection glass of photovoltaic systems", Prog. Photovoltaics Res. Appl., vol. 19, no 3, pp. 339-344, 2011.
6. P. Chartier, M.-J. Azzopardi, N. Codazzi, P. Chaussade, Y. Naoumenko, F. Gauthier and O. Guiselin, "Multilayered hydrophobic window glass", US Patent 5 800 918, Sep. 1, 1998.
7. A. Solga, Z. Cerman, B.F. Striffler, M. Spaeth and W. Barthlott, "The dream of staying clean: lotus and biomimetic surfaces", Bioinspir. Biomim., vol 2, no 4, p. S126, 2007.
8. M. Madhup, N. Shah and P. Wadhwani, "Investigation of surface morphology, anti-corrosive and abrasion resistance properties of nickel oxide epoxy nanocomposite (NiO-ENC) coating on mild steel substrate", Prog. Org. Coa., vol. 80, pp. 1-10, 2015.
9. P. Wang, D. Zhang, R. Qiu and B. Hou, "Super-hydrophobic film prepared on zinc as corrosion barrier", Corros. Sci., vol. 53, no 6, pp. 2080–2086, 2011.
10. L. Gao and T.J. McCarthy, ""Artificial lotus leaf" prepared using a 1945 patent and a commercial textile", Langmuir, vol. 22, no 14, pp. 5998–6000, 2006.
11. B. Roe and X. Zhang, "Durable hydrophobic textile fabric finishing using silica nanoparticles and mixed silanes", Text. Res. J., vol. 79, no 12, pp. 1115–1122, 2009.
12. D.-Y. Kim, J.-G. Lee, B.N. Joshi, S.S. Latthe, S.S. Al-Deyab and S.S. Yoon, "Self-cleaning superhydrophobic films by supersonic-spraying polytetrafluoroethylene-titania nanoparticles", J. Mater. Chem. A, vol. 3, no 7, pp. 3975–3983, 2015.
13. A. Vorobyev and C. Guo, "Multifunctional surfaces produced by femtosecond laser pulses", J. Appl. Phys., vol. 117, no 3, p. 033103, 2015.
14. N.V. Motlagh, F.C. Birjandi, J. Sargolzaei and N. Shahtahmassebi, "Durable, superhydrophobic, superoleophobic and corrosion resistant coating on the stainless steel surface using a scalable method", Appl. Surf. Sci., vol. 283, pp. 636–647, 2013.
15. H. Wang, E. Chen, X. Jia, L. Liang and Q. Wang, "Superhydrophobic coatings fabricated with polytetrafluoroethylene and SiO2 nanoparticles by spraying process on carbon steel surfaces", Appl. Surf. Sci., vol. 349, pp. 724–732, 2015.
16. E.J. Park, J.K. Sim, M.-G. Jeong, H.O. Seo and Y.D. Kim, "Transparent and superhydrophobic films prepared with polydimethylsiloxane-coated silica nanoparticles", RSC Adv., vol. 3, no 31, pp. 12571–12576, 2013.
17. Z. Lin, Y. Liu and C.-p. Wong, "Facile fabrication of superhydrophobic octadecylamine-functionalized graphite oxide film", Langmuir, vol. 26, no 20, pp. 16110–16114, 2010.

18. D.D. Nguyen, N.-H. Tai, S.-B. Lee and W.-S. Kuo, “Superhydrophobic and superoleophilic properties of graphene-based sponges fabricated using a facile dip coating method”, Energy Environ. Sci., vol. 5, no 7, pp. 7908–7912, 2012.
19. Y. Lin, G.J. Ehlert, C. Bukowsky and H.A. Sodano, “Superhydrophobic functionalized graphene aerogels”, ACS Appl. Mater. Interfaces, vol. 3, no 7, pp. 2200–2203, 2011.
20. J. Rafiee, M.A. Rafiee, Z.-Z. Yu and N. Koratkar, “Superhydrophobic to superhydrophilic wetting control in graphene films”, Adv. Mater., vol. 22, no 19, pp. 2151–2154, 2010.
21. M.J. Nine, M.A. Cole, L. Johnson, D.N. Tran and D. Losic, “Robust superhydrophobic graphene-based composite coatings with self-cleaning and corrosion barrier properties”, ACS Appl. Mater. Interfaces, vol. 7, no 51, pp. 28482–28493, 2015.
22. H.O. Pierson, “Handbook of Carbon, Graphite, Diamonds and Fullerenes: Processing, Properties and Applications”, William Andrew, 2012.
23. D. Kwok, T. Gietzelt, K. Grundke, H.-J. Jacobasch and A.W. Neumann, “Contact angle measurements and contact angle interpretation. 1. Contact angle measurements by axisymmetric drop shape analysis and a goniometer sessile drop technique”, Langmuir, vol. 13, no 10, pp. 2880–2894, 1997.
24. A.C. Ferrari and J. Robertson, “Interpretation of Raman spectra of disordered and amorphous carbon”, Phys. Rev. B, vol. 61, no 20, p. 14095, 2000.
25. F. Tuinstra and J.L. Koenig, “Raman spectrum of graphite”, J. Chem. Phys., vol. 53, no 3, pp. 1126–1130, 1970.
26. A.C. Ferrari, “Raman spectroscopy of graphene and graphite: disorder, electron-phonon coupling, doping and nonadiabatic effects”, Solid State Commun., vol. 143, no 1, pp. 47–57, 2007.
27. K. Tadanaga, J. Morinaga, A. Matsuda and T. Minami, “Superhydrophobic-superhydrophilic micropatterning on flowerlike alumina coating film by the sol- gel method”, Chem. Mater., vol. 12, no 3, pp. 590–592, 2000.
28. L. Liu, Y. Chen and P. Huang, “Preparation and tribological properties of organically modified graphite oxide in liquid paraffin at ultra-low concentrations”, RSC Adv., vol. 5, no 110, pp. 90525–90530, 2015.
29. Y. Yang, C.-E. He, W. Tang, C.P. Tsui, D. Shi, Z. Sun, T. Jiang and X. Xie, “Judicious selection of bifunctional molecules to chemically modify graphene for improving nanomechanical and thermal properties of polymer composites”, J. Mater. Chem. A, vol. 2, no 47, pp. 20038–20047, 2014.

Proceedings of SurfCoat Korea 2018 International Conference
Incheon, Rep. Of Korean, March 28 - 30, 2018
DOI: https://doi.org/10.26799/cp-surfcoatkorea2018

Effect of annealing Nickel feedstock powder to produce WC-5wt%Ni cold sprayed coatings

Tatenda Chingosho[1, 2], Natasha Sacks[1, 2], Ionel Botef[2, 3]

[1]School of Chemical and Metallurgical Engineering, University of the Witwatersrand, Johannesburg, Private Bag 3, Wits 2050, South Africa
[2]DST-NRF Centre of Excellence in Strong Materials, South Africa
[3]School of Mechanical, Industrial and Aeronautical Engineering, University of the Witwatersrand, South Africa

Abstract
A low pressure cold spray system was used to deposit WC-5wt%Ni coatings onto mild steel substrates. In order to improve coating deposition, the Ni powder was annealed prior to being milled with the WC powder, and the coatings were compared to coatings based on pre-annealed Ni powder. The microstructures were characterized and the slurry abrasion resistance tested. Annealing the Ni powder produced thicker coatings of 255 ± 3 µm compared to 28.5 ± 1 µm measured for the coatings using pre-annealed Ni powder. However the coatings produced using the annealed Ni powder had a lower retention of WC (43±0.7% compared to 58±9%), a larger WC grain size (1.83±0.004µm compared to 0.16±0.06) and a lower hardness (361±83$HV_{0.3}$ compared to 470±9$HV_{0.3}$) compared to the coatings produced using the pre-annealed Ni powder. The porosity levels of the annealed Ni-based coating were lower at 0.65±0.32% compared to 6.45±2.64%. During slurry abrasion the annealed Ni-based coatings showed a better wear resistance compared to the pre-annealed Ni-based coatings despite having a lower hardness. The wear mechanisms for both coatings were similar. Research is still on-going to fully understand the effect of using the annealed Ni powder to produce the coatings.

Keywords: cold spray, cemented carbides, tungsten, nickel, slurry abrasion

1. Introduction

Pipelines used in different industries experience various types of failure during their operational lifetime which influences operational efficiency [1]. Pipeline fracture and failure by slurry abrasion is a common problem, especially in the mining industry [1]. Prolonged interaction of the hard protuberances carried in the pipeline medium with the pipeline interior leads to material degradation which compromises the surface integrity and facilitates failure. Typically steels are used to manufacture pipelines, and in an attempt to combat slurry abrasion wear, thermally sprayed cemented tungsten carbide (WC) coatings have been employed due to their excellent abrasion resistance [1–3]. To date cold gas dynamic sprayed (CGDS) WC-based coatings have not been used in pipelines. Cold spraying is a process in which solid particles are accelerated in a de Laval nozzle toward a substrate [3]. If the impact velocity exceeds some threshold value, then the powder particles experience plastic deformation and adhere to the substrate surface, thereby forming a coating. Due to the low temperatures experienced during deposition there is limited risk of decarburization, oxidation, and undesirable phase formation during deposition [4–8]. The physical and mechanical properties of these cold sprayed coatings have been shown to be similar and in some instances better than those produced by high temperature processes [9]. It is well known that the feedstock powder properties influence the deposition kinetics and the resultant properties of a coating [9–12]. Hence in the current study an attempt was made to enhance plastic deformation of the feedstock powder by annealing the nickel powder, selected as the binder to cement the WC, prior to deposition. The slurry abrasion resistance of the coatings produced using the annealed powder was compared to that of coatings produced using pre-annealed powder.

2. Experimental

2.1 Materials

A gas atomized Ni powder (34 µm, Praxair Surface Technologies) and a WC powder (4 µm, Metal-Tech Ltd) were used as feedstock powders to produce WC-5wt%Ni coatings on mild steel substrates (18 x 18 x 4 mm) which had been grit blasted with alumina. Prior to being blended, the Ni powder was annealed in a tube furnace at 500 °C for 4 hrs. The powder particle size distributions were determined using a Malvern Mastersizer 2000. The coatings were fabricated using a low

DOI: https://doi.org/10.26799/cp-surfcoatkorea2018

pressure cold spray machine (Centreline, Canada) with optimised deposition parameters of 12.1 bar pressure, a 15 mm stand-off distance, 30% powder feed rate and a deposition temperature of 500 °C. For comparison purposes coatings were also produced using pre-annealed Ni powder.

2.2 Microstructural Characterization

The coatings were polished to a 1 µm surface finish in order to evaluate the microstructural properties. Phase analyses of the powders and coatings were done using a Bruker D2 X-ray diffraction (XRD) machine and its associated EVA Software. The coating thicknesses were measured from images captured using both an Olympus BX63 optical microscope (OM) and a Carl Zeiss Sigma Field Emission Scanning Electron Microscope (FESEM). The morphology of both powders and coatings were studied using FESEM, and images were used for lineal analyses to determine the WC grain size and coating porosity. Elemental mappings were done using an Oxford x-act energy dispersive X-ray spectrometer (EDS) attached to the FESEM. Vickers hardness measurements were done according to ASTM C1237 [13] using a 300 gf indenting load with a dwell time of 10 s.

2.3 Slurry Abrasion Tests

Slurry abrasion tests were conducted on the coatings according to ASTM B611-91 [14]. Silica sand with an angular morphology was used as the abrasive medium. For the annealed Ni-based coatings, the test duration was 6 hours and mass loss measurements were taken every hour. For the pre-annealed Ni-based coatings, the test duration was 30 minutes and mass loss measurements were taken every 5 minutes. The difference in test duration was based on coating thickness. The wear scars were examined using FESEM in order to identify the wear mechanisms.

3. Results & Discussion

3.1 Annealing of gas atomized Ni powder

The post-annealed Ni powder showed a similar spherical morphology as the pre-annealed Ni powder (Fig.1) suggesting that the annealing did not have significant effect on the shape of the powder particles. Raman spectroscopy (Fig 2.a) showed a thin NiO film on the surface of the post-annealed Ni powder; the strongest signal was on a d-spectrum (at 500 cm^{-1}). EDS analysis showed a 76% increase in oxygen content of the post-annealed Ni powder. This trait was also reported by Valladares et al [15]. Fig 2.b shows the XRD patterns of the Ni powder before and after annealing with no new phases detected, nor any peak broadening. However there was a reduction in peak intensity observed on the heat treated Ni XRD pattern, which can be attributed to the formation of the NiO film.

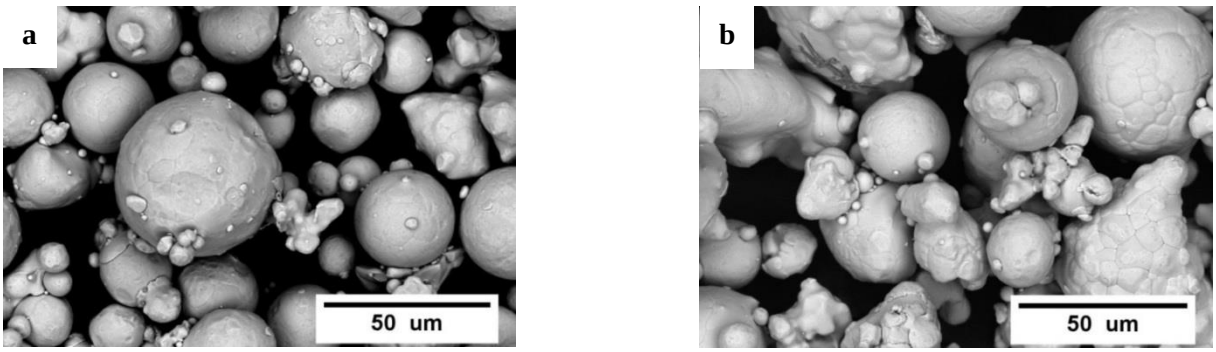

Figure 1: FESEM micrographs showing powder morphologies of Ni powder (a) pre-annealed and (b) post-annealed.

Proceedings of SurfCoat Korea 2018 International Conference
Incheon, Rep. Of Korean, March 28 - 30, 2018
DOI: https://doi.org/10.26799/cp-surfcoatkorea2018

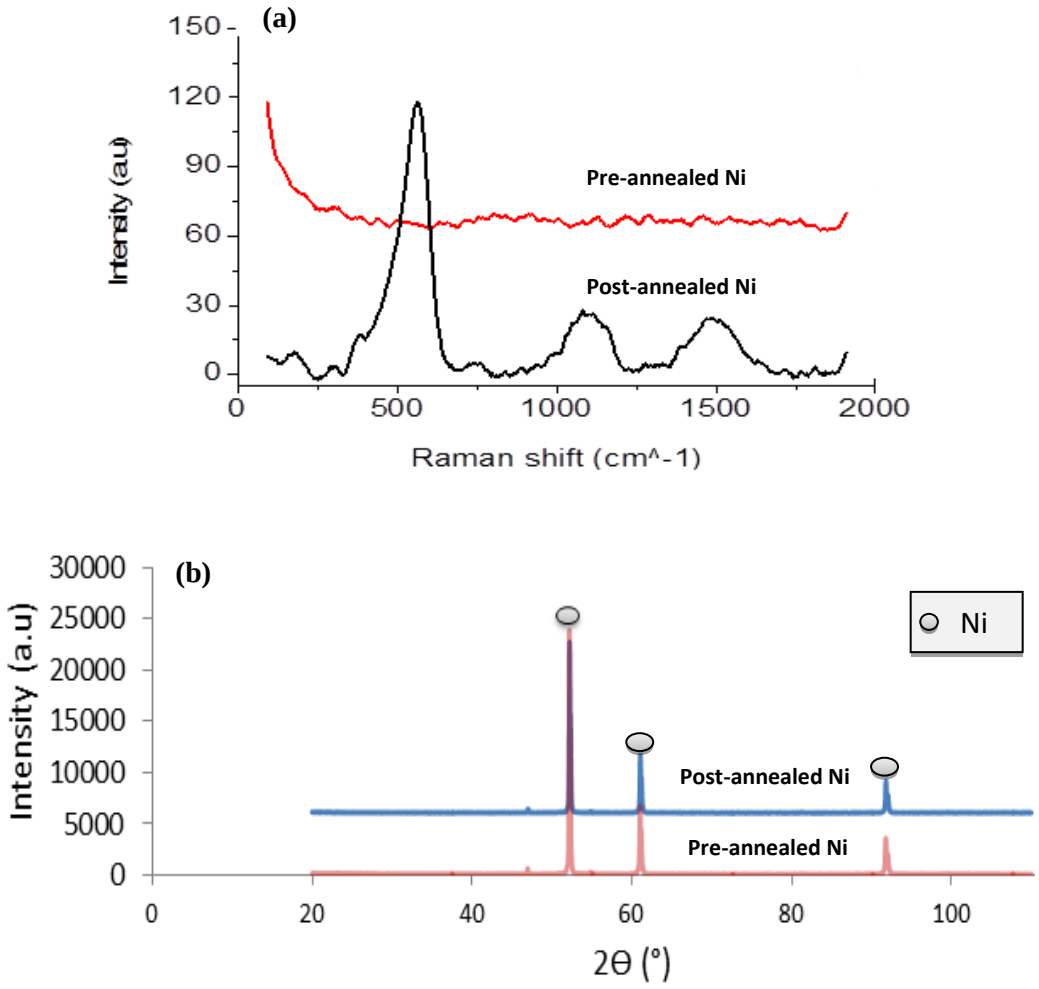

Figure 2: (a) Raman spectra and (b) XRD patterns for Ni powders.

Fig.3 shows the WC-5wt%Ni coating microstructures based on the pre-annealed Ni (Fig. 3.a) and post-annealed Ni (Fig. 3.b) powders. The coating produced using the pre-annealed Ni was thin and non-homogenous with more pores when compared to the coating produced using the annealed Ni powder. Annealing the Ni created a more homogenous and thicker (89% increase) coating with less porosity. These improved deposition characteristics are likely due to the lower hardness measured for the annealed Ni powders of 29 ± 28 $HV_{0.3}$ compared to a hardness of 56 ± 51 $HV_{0.3}$ for the pre-annealed Ni powder. The decrease in hardness allowed for more plastic deformation during deposition which also resulted in better coating build-up.

Table 1 lists the properties of the coatings produced using the two different Ni powders. The coating produced using the annealed Ni powder had a lower retention of WC particles, a larger WC grain size, lower porosity, and a lower hardness compared to the coating produced using the pre-annealed Ni powder.

DOI: https://doi.org/10.26799/cp-surfcoatkorea2018

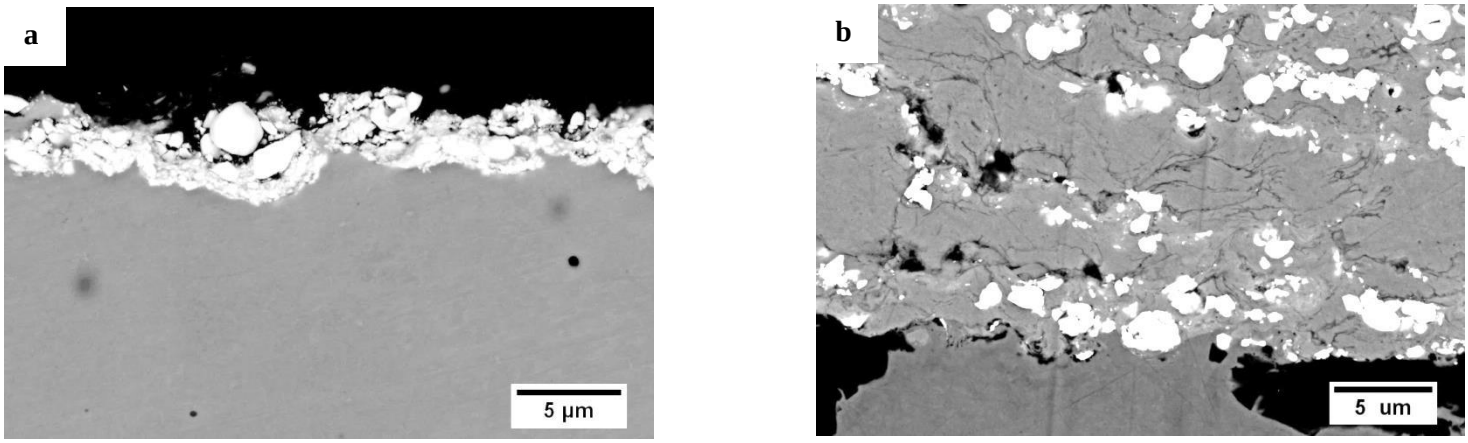

Figure 3: FESEM images showing WC-5wt%Ni coating microstructures based on (a) pre-annealed Ni and (b) post-annealed Ni.

Table 1: Coating properties.

WC-5wt%Ni coating properties	**Pre-annealed Ni**	**Post-annealed Ni**
WC retained (wt%)	57.8 ± 9 %	42.9 ± 0.7
WC grain size (µm)	0.16 ± 0.06	1.04 ± 1.11
Thickness (µm)	29 ± 1	255 ± 3
Porosity (%)	6.45 ± 2.64	0.65 ± 0.32
Hardness ($HV_{0.3}$)	470 ± 9	361 ± 83

3.2 Slurry abrasion wear

Fig. 4.a shows the mass loss curves of the two coatings from the slurry abrasion tests while Fig. 4.b shows the silica sand which was used as the abrasive. The applied stress during abrasion was approximately 0.07 MPa. Both coatings show an initial increase in mass loss within the first few minutes of testing followed by a slowing down in the wear rate. The respective Ha/Hs ratios for each coating are also shown (Ha = hardness of abrasive; Hs = hardness of sample). The Ha/Hs ratios indicate whether the coatings experience hard abrasion or soft abrasion as defined by Hutchings [16]. Based on the ratios of 3.4 and 3.81 for the pre-annealed Ni-based coatings and post-annealed Ni-based coatings respectively, both coatings experienced hard abrasion. The wear rates for each coating are 3.1 ± 0.26 mg/min and 0.4 ± 0.06 mg/min, with the pre-annealed Ni-based coatings having the higher wear rate. This was a surprising result given that the pre-annealed Ni-based coatings had a smaller WC grain size and higher hardness compared to the post-annealed Ni-based coatings. Fig. 5 shows high magnification images of the worn surfaces for both coatings after being subjected to slurry abrasion. More scratches, cracks and smearing were observed in the pre-annealed Ni-based coatings compared to the post-annealed Ni-based coatings, which experienced similar wear mechanisms but to a lesser extent. Both coatings exhibited features of the equal pressure theory [7] where portions of, or even the entire reinforcing particles were removed from the Ni matrix.

DOI: https://doi.org/10.26799/cp-surfcoatkorea2018

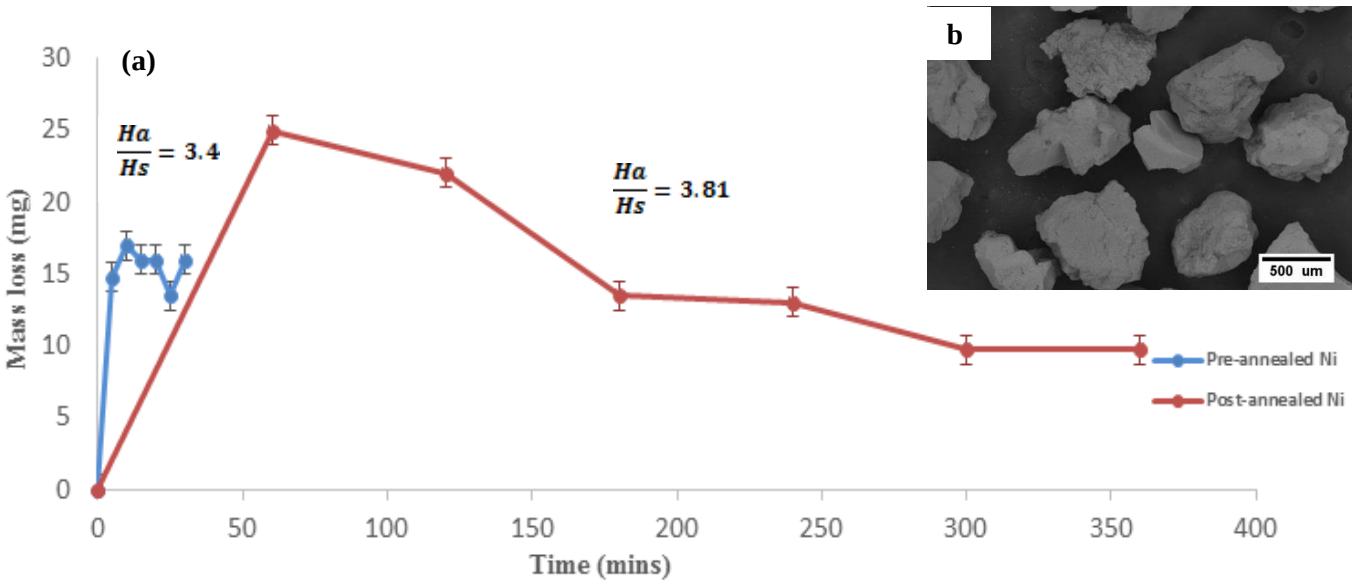

Figure 4: (a) Mass loss curves of WC-5wt%Ni coatings and (b) silica sand used in the slurry abrasion tests.

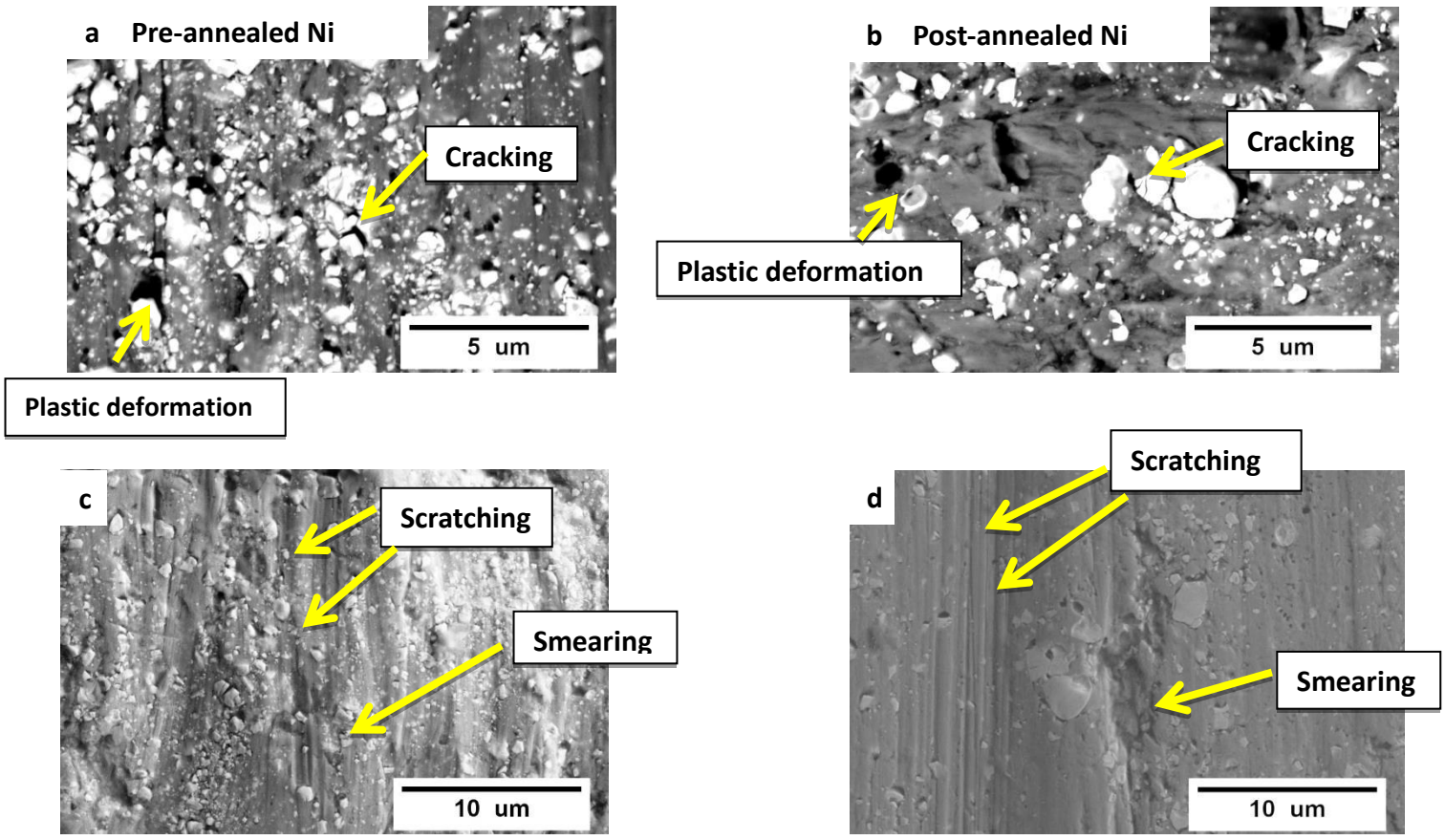

Figure 5: FESEM images of worn surfaces of (a & c) pre-annealed Ni-based coatings and (b & d) post-annealed Ni-based coatings.

DOI: https://doi.org/10.26799/cp-surfcoatkorea2018

4. Conclusions

Annealing the Ni feedstock powder improved the deposition characteristics of the WC-5wt%Ni coating. This was likely due to the lower hardness of the annealed Ni powder which allowed for greater plastic deformation during deposition. A thickness increase of approximately 89% was measured for the coatings produced using the annealed Ni powder compared to the coatings produced using the pre-annealed Ni powder. The coating produced using the annealed Ni powder had a lower retention of WC particles, a larger WC grain size and lower porosity compared to the coating produced using the pre-annealed Ni powder. Annealing led to improved slurry abrasion resistance. Further work is being done to fully understand the effects of using the annealed Ni powder to produce the coatings.

Acknowledgements

The authors wish to acknowledge the Department of Science and Technology and the National Research Foundation in South Africa for their financial support. Pilot Tools Pty Ltd, South Africa is acknowledged for the use of their facilities. The support of all technical staff involved in this work is acknowledged.

References

[1] Magagula NBS, Sacks N, Botef I. Slurry abrasion of WC-4wt % Ni cold- sprayed coatings in synthetic minewater 2016;116:333–7.
[2] Karimi A, Verdon C, Barbezat G. Microstructure and hydroabrasive wear behaviour of high velocity oxy-fuel thermally sprayed WCCo(Cr) coatings. Surf Coatings Technol 1993;57:81–9.
[3] Moridi A, Hassani-Gangaraj SM, Guagliano M, Dao M. Cold spray coating: review of material systems and future perspectives. Surf Eng 2014;30:369–95.
[4] Siao A, Ang M, Berndt CC, Cheang P. Surface & Coatings Technology Deposition effects of WC particle size on cold sprayed WC – Co coatings. Surf Coat Technol 2011;205:3260–7.
[5] Cavaliere P, Perrone A, Silvello A. Processing Conditions Affecting Grain Size and Mechanical Properties in Nanocomposites Produced via Cold Spray. J Therm Spray Technol 2014;23:1089–96.
[6] Melendez NM, Narulkar V V, Fisher GA, Mcdonald AG. Effect of reinforcing particles on the wear rate of low-pressure cold-sprayed WC-based MMC coatings. Wear 2013;306:185–95.
[7] Lioma D, Sacks N, Botef I. Cold gas dynamic spraying of WC–Ni cemented carbide coatings. Int J Refract Met Hard Mater 2015;49:365–73.
[8] Nunthavarawong P, Sacks N, Botef I. Effect of Substrate Type on the Material Properties of WC-5wt % Ni Cold Sprayed Coatings. Conf. World PM2016 Congr. ProceedingsAt Hamburg, Ger. by Eur. Powder Metall. Assoc., 2016, p. 1–6.
[9] Ji GC, Wang HT, Chen X, Bai XB, Dong ZX, Yang FG. Characterization of cold-sprayed multimodal WC-12Co coating. Surf Coatings Technol 2013;235:536–43.
[10] Luo X, Li Y, Li C. A comparison of cold spray deposition behavior between gas atomized and dendritic porous electrolytic Ni powders under the same spray conditions. Mater Lett 2016;163:58–60.
[11] Fauchais P, Vardelle A. Thermal Sprayed Coatings Used Against Corrosion and Corrosive Wear. n.d.
[12] Winnicki M, Ma A, Rutkowska-gorczyca M, Soko P, Ambroziak A, Paw L. Surface & Coatings Technology Characterization of cermet coatings deposited by low-pressure cold spraying. Surf Coat Technol 2015;268:108–14.
[13] ASTM C1327 - Standard Test Method for Vickers Indentation Hardness of Advanced Ceramics | Engineering360 n.d. http://standards.globalspec.com/std/9905618/astm-c1327 (accessed February 2, 2017).
[14] ASTM E384 Standard Test Method for Knoop and Vickers Hardness of Materials. ASTM Int 2016. www.astm.org, West Conshohocken (accessed July 9, 2016).
[15] De Los Santos Valladares L, Ionescu A, Holmes S, Barnes CHW, Bustamante Domínguez A, Avalos Quispe O, et al. Characterization of Ni thin films following thermal oxidation in air. J Vac Sci Technol B, Nanotechnol Microelectron Mater Process Meas Phenom 2014;32:51808.
[16] Hutchings LM. Triblology: Friction and wear of engineering materials. CRC Press London 1992:273.